Nanoscale Organization of Conjugated Rods in Rod–Coil Molecules**

By *Myongsoo Lee*,* *Jung-Woo Kim*, *In-Wook Hwang*, *Yong-Rok Kim*, *Nam-Keun Oh*, and *Wang-Cheol Zin*

An important challenge in the preparation of self-assembling materials is the control of supramolecular structure with well-defined shape and size, which has potential implications both fundamentally and practically in areas such as materials science, molecular electronics, and biomimetic chemistry.[1–3] A typical example of a self-assembling system is provided by rod–coil molecules consisting of stiff rod and flexible coil segments. The repulsion between the covalently connected rod and coil segments leads to self-organization into a variety of supramolecular structures whose shape and size are determined by the relative volume fraction of the rod block.[4,5]

Recent observations from our laboratory have shown that both rod–coil diblock molecules and rod–coil multiblock copolymers containing poly(propylene oxide) as a coil segment self-assemble into layered smectic, bicontinuous cubic, and hexagonal columnar liquid-crystalline superlattices as the coil segment of the molecule increases in length relative to the rod segment.[6] In a preliminary communication,[7] we have demonstrated that introduction of a hydrophobic docosyl chain into the rod–coil diblock molecule based on the hydrophilic poly(ethylene oxide) coil gives rise to the formation of a discrete micellar phase with a lack of three-dimensional (3D) symmetry. In a more recent publication, rod–coil ABA triblock molecules based on poly(propylene oxide) as the coil segment were proved to self-assemble into discrete rod bundles that organize into a 3D tetragonal structure.[8]

Our approach to controlling supramolecular architecture can be extended to rod–coil systems based on a conjugated rod, which create a novel class of self-assembling materials with unique optical and electronic properties. As a result of great interest in the optically and electronically active properties of highly conjugated and stiff rod-like molecules, a variety of oligomers and polymers have been synthesized to establish the molecular structure–property relationship.[9,10] Recently, however, supramolecular structure as well as chain structure has been reported to have a dramatic effect on the physical properties of conjugated molecules.[11–14] Thus, manipulation of supramolecular structure in conjugated molecules is of paramount importance in achieving efficient physical properties in solid-state molecular materials. A strategy to manipulate the supramolecular structure may be accessible by incorporation of the conjugated rod into a rod–coil architecture, which would allow formation of well-defined electronically and optically active 2D sheet-like, strip-like, and hockey puck cylinder-like domains in nanoscale dimensions.

It is in this context that we have synthesized coil–rod–coil triblock molecules consisting of three biphenyls connected through vinylene linkages as a conjugated rod segment and poly(propylene oxide) (PPO) as the coil segment. The synthesis of coil–rod–coil molecules with a variety of coil lengths was performed as outlined in Scheme 1. Monophenylbenzyl alcohol-terminated PPOs **1**–**5** were prepared from the reaction of

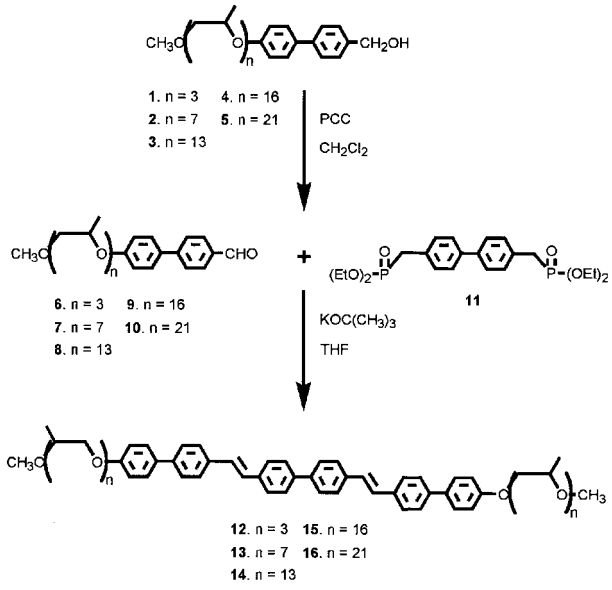

Scheme 1. Synthesis of coil–rod–coil molecules.

the appropriate monotosylated PPO with an excess amount of 4′-hydroxy-4-biphenyl methylene alcohol according to the procedure reported previously.[6] Oxidation of the resulting **1**–**5** with pyridinium chlorochromate (PCC) then produced compounds **6**–**10** with an aldehyde functional group. The coil–rod–coil molecules **12**–**16** were obtained by treating the corresponding presursor molecules **6**–**10** with bis(diethylphosphonate) derivative **11** in the presence of potassium *tert*-butoxide according to the Wittig-Horner reaction.[15] The resulting coil–rod–coil molecules were purified by column chromatography (silica gel) using ethyl acetate as the eluent. The trans selectivity of the Wittig–Horner reaction is sufficiently high to generate all-trans isomers **12**–**16** within the limits of NMR detection. Details of the synthesis and characterization can be found in the Experimental section. All of the coil–rod–coil molecules showed a narrow molecular weight distribution with polydispersity index of less than 1.07, as determined from gel permeation chromatography (GPC) relative to polystyrene standards (Table 1).

The solid-state organization behavior of the coil–rod–coil molecules was characterized by polarized optical microscopy,

[*] Prof. M. Lee, J.-W. Kim, I.-W. Hwang, Prof. Y.-R. Kim
Department of Chemistry, Yonsei University
Shinchon 134, Seoul 120-749 (Korea)
E-mail: mslee@alchemy.yonsei.ac.kr
N.-K. Oh, Prof. W.-C. Zin
Department of Materials Science and Engineering
Pohang University of Science and Technology
Pohang 790-784 (Korea)

[**] This work was supported by CRM-KOSEF (2000), the Korea Science and Engineering Foundation (1999-1-308-002-3), and Pohang Accelerator Laboratory, Korea. JWK acknowledges the BK 21 fellowship from the Ministry of Education, Korea.

  0935-9648/01/1809-1363 $ 17.50+.50/0

ADVANCED MATERIALS

Table 1. Characterization of coil–rod–coil molecules by GPC, DSC, and SAXS.

molecule	M_w/M_n [a]	T_m (°C) and corresponding enthalpy changes (kJ/mol)	Lamellar	Columnar		Body-centered tetragonal				density (g/cm^3)		number of molecules in a micelle
								Lattice constant				
		heating	d_{100} (Å)	d_{100} (Å)	Lattice constant (a) (Å)	d_{101} (Å)	d_{002} (Å)	a (Å)	c (Å)	ρ [c]	ρ_{rod} [d]	n [e]
12	1.02	k 345 [b] dec [f]	38.5							1.130	1.262	
13	1.03	k 324.8 (1.6) i		53.5	62.0					1.097	1.259	
14	1.07	k 234.3 (1.5) i				56.6	38.3	83.3	76.6	1.054	1.247	82
15	1.07	k 182.4 (1.7) i				63.5	43.0	93.7	86.1	1.046	1.244	83
16	1.06	k 180.7 (2.1) i				69.0	45.2	98.3	90.4	1.035	1.234	85

[a] Determined from GPC. [b] k = crystalline, i = isotropic. [c] ρ = molecular density. [d] ρ_{rod} = rod density. [e] Number of molecules in each micelle $n = a^2cN_A\rho/(2M)$, where M = molecular weight, ρ = molecular density, and N_A = Avogadro's number. [f] dec = decomposition.

differential scanning calorimetry (DSC), and X-ray scattering measurements. All of the coil–rod–coil molecules are viscoelastic waxes whose stiffness decreases with increasing coil length. Between crossed polarizers, these waxy solids show strong birefringence, which disappears over a very narrow temperature range upon heating. As expected, the melting transition of the coil–rod–coil molecules is observed to decrease as the PPO coil length increases (Table 1).

The solid-state structure of the coil–rod–coil molecules was identified by small- and wide-angle X-ray scattering (SAXS and WAXS) measurements. As shown in Figure 1, the SAXS pattern of coil–rod–coil molecule **12** with the shortest coil length shows a sharp primary reflection together with a weak reflection at a higher angle with q-spacing ratio of 1:2. Therefore, the primary reflection can be indexed as the (001) plane of the lamellar structure with a layer thickness of 38.8 Å. At wide angles a sharp reflection with low intensity at q-spacing of 14.0 nm^{-1} is observed (Fig. 2), presumably corresponding to crystal packing of the rod segments within the aromatic domain with an average inter-rod distance of 4.5 Å. These results indicate that **12** is self-assembled into a lamellar structure consisting of nanophase separated crystalline rod domains and amorphous coil domains. The observed layer spacing of 38.8 Å corresponds to a rod tilt at an angle of 47° relative to the layer normal, considering the extended molecular length of 58 Å.

The SAXS pattern of **13** shows three sharp reflections at q-spacings of 1.17, 2.04, and 2.36 nm^{-1} (Fig. 1). The relative positions of these reflections are 1, 3, and 4, which can be indexed as the 100, 110, and 200 reflections of a 2D hexagonal structure with a lattice constant of 62.0 Å.[6] Taking into account the lattice constant and density, the inner core of the

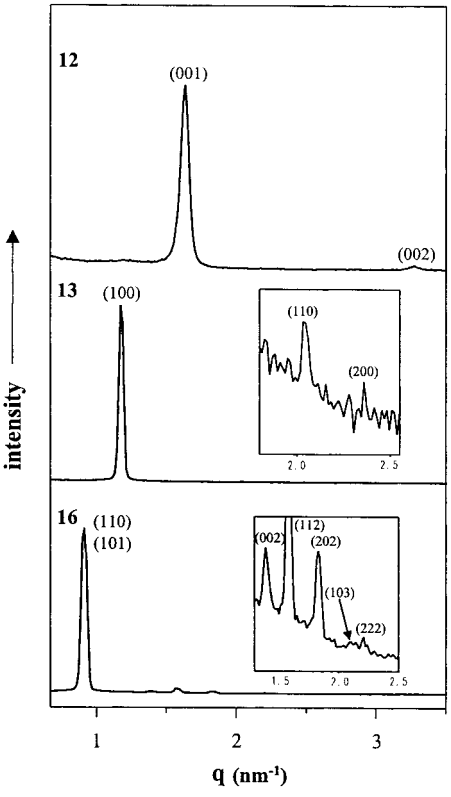

Fig. 1. Small-angle X-ray diffraction patterns of **12**, **13**, and **16** measured at room temperature.

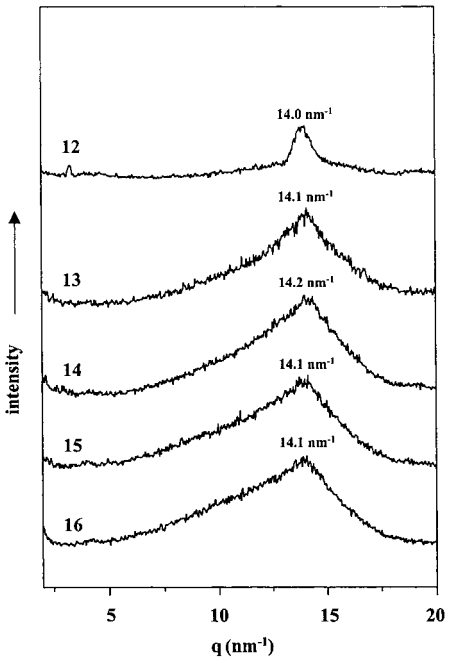

Fig. 2. Wide-angle X-ray diffraction patterns of **12**–**16** measured at 25 °C.

  0935-9648/01/1809-1364 $ 17.50+.50/0

column consists of rod segments, while the outer part consists of PPO coils that splay to fill the inter-columnar matrix.

In contrast, **14**–**16**, with longer PPO coils, show a large number of sharp reflections in the small-angle range, suggestive of 3D order. As shown in Figure 1, the SAXS patterns of these molecules show a sharp, high-intensity reflection at low angles together with a number of sharp reflections of low intensity at higher angles. Similar to the result from our laboratory described previously,[8] the observed reflections can be indexed as (110), (010), (002), (112), (202), (103), and (222) planes of a 3D body-centered tetragonal lattice with c/a = 0.92. The WAXS patterns of these molecules (Fig. 2) show a reflection at q-spacing of about 14.1 nm^{-1}, which is due to crystal packing of rod segments within the aromatic domains. The observed d-spacings and lattice constants are summarized in Table 1.

Considering that the 3D tetragonal structure consists of discrete supramolecular nanostructures, the inner core is constituted by a discrete rod-bundle that is encapsulated by PPO coils. The lattice constants and measured densities suggest that for **14**–**16** the average number (n) of molecules is approximately 83 in each supramolecular aggregate (Table 1). Considering that the long axes of the rod segments are aligned parallel to each other, the aggregation of 83 rod segments in a nanostructure can be estimated to generate a rod-bundle with a hockey-puck-like cylindrical shape. This shape of the aromatic domain seems to be responsible for the formation of non-spherical aggregates that organize into an unusual 3D tetragonal superlattice. On the basis of the results described so far, the possible models for the generation of the lamellar, 2D hexagonal, and 3D tetragonal structures can be illustrated as in Figure 3.

The solid-state absorption spectra of all the coil–rod–coil molecules exhibit an intense transition with a maximum at 350 nm (Fig. 4, left) resulting from the conjugated rod block. Solid films of these molecules give a brilliant blue fluorescence. The solid-state fluorescence spectra of the coil–rod–coil molecules excited at 350 nm exhibit a strong fluorescence with a maximum at 479 nm (Fig. 4, right), corresponding to blue light emission upon excitation. The suitability of the coil–rod–coil molecule for applications depends on the ability of the rod to function as an efficient fluorescent block in the solid state. As described earlier, the supramolecular structure is crucial to this function. The efficiency of fluorescence may be estimated from the extent to which emission from the rod block is suppressed. In this regard, a picosecond time-correlated single-photon counting system was employed for time-resolved fluorescence decay measurements of the coil–rod–coil molecules in the solid state (Fig. 5). The total mean fluorescence lifetimes (τ_m) measured over the 400–650 nm range for **12**, **13**, **14**, and **16** are summarized in Table 2.[16]

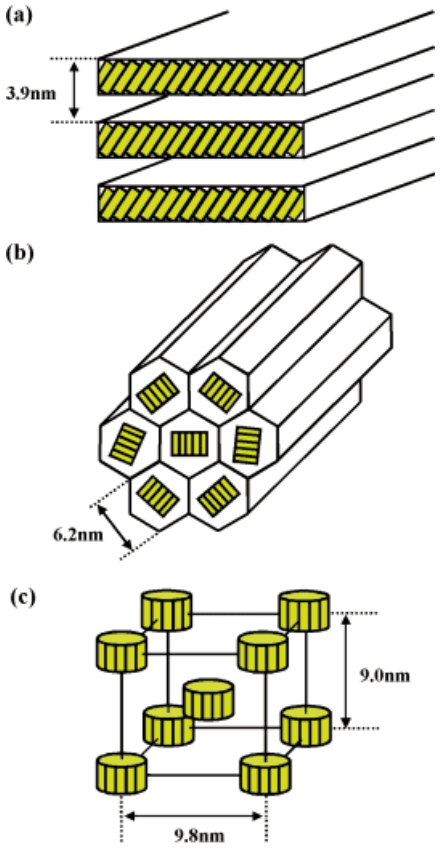

Fig. 3. Schematic representation of a) the lamellar structure of **12**, b) the 2D hexagonal structure of **13**, and c) the 3D tetragonal structure of **16**.

Remarkably, the time-resolved fluorescence decay appears to depend strongly on the supramolecular structure. As shown in Table 2, the mean fluorescence lifetime of **13**, which is self-assembled into a 2D hexagonal structure, is very close to that of **12**, which has a lamellar structure. In contrast, a notable enhancement of the mean lifetime is observed in both **14** and **16**,

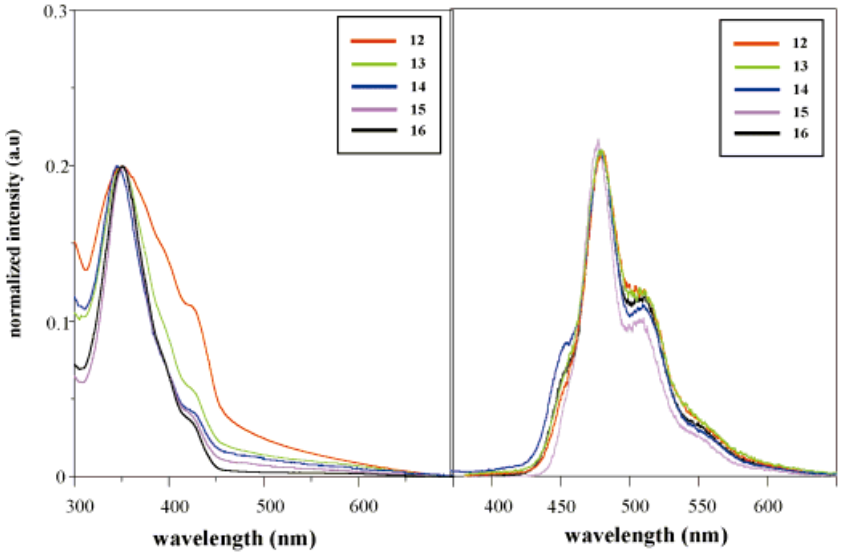

Fig. 4. UV-vis absorption (left) and fluorescence (right) spectra of **12**–**16** in the solid state.

  0935-9648/01/1809-1365 $ 17.50+.50/0

ADVANCED MATERIALS

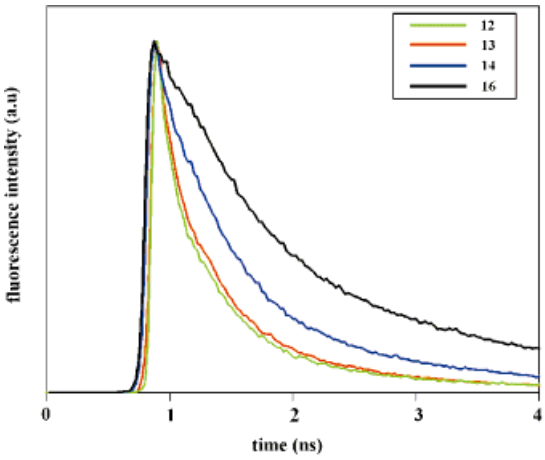

Fig. 5. Fluorescence decay dynamics of **12**, **13**, **15**, and **16** when excited at 350 nm and monitored at 480 nm.

Table 2. Summary of time-resolved fluorescence decay dynamics data [a].

molecule	total mean fluorescence lifetime (τ_m) (400-650nm)
12	0.42 ns
13	0.43 ns
14	0.73 ns
16	1.21 ns

[a] Obtained from picosecond time-correlated single-photon counting (TCSPC) measurements.

which are assembled into a 3D tetragonal structure. The mean lifetime is highest in **16** with $\tau_m = 1.21$ ns, which is nearly three times that of **12** and **13**.

This result can be rationalized in terms of the optically active rod domain nanostructure. As shown in Figure 3, the supramolecular structure of **14** and **16** consists of three-dimensionally confined rod domains encapsulated by PPO coil segments, in contrast to those of **12** and **13**, where the rods are assembled into two- (sheet-like) and one- (strip-like) dimensionally continuous domains, respectively. Therefore, this 3D confinement of conjugated rod domain is presumably responsible for the enhancement in the mean fluorescence lifetime in the case of **14** and **16**.[18] In addition, the enhanced fluorescence lifetime in **16** compared to **14** is attributed to the increase in the distance between adjacent rod-bundles as evidenced by the previously discussed X-ray results (Table 1). Isolation and confinement of the conjugated polymer chains into nanochannels have been reported to result in fluorescence enhancement.[14] The definitive feature of the driving forces responsible for the variation in fluorescence behavior depending on the supramolecular structure and inter-bundle distance is the subject of ongoing investigations. However, these results indicate that the three-dimensionally confined nanodomains provide a substantially different local environment for conjugated rods.

In summary, the rod–coil molecules based on a conjugated rod were observed to be self-organized into successively 1D lamellar, 2D hexagonal, and 3D tetragonal supramolecular structures with increasing coil-to-rod volume fraction. All of the rod–coil molecules showed a brilliant blue emission with fluorescence maximum at 479 nm. The time-resolved fluorescence decay dynamics showed that the fluorescence behavior of the rod–coil molecules is strongly dependent on supramolecular structure. The mean fluorescence lifetime of **13**, which has a 2D hexagonal structure, is similar to that of **12**, which shows a lamellar structure. Remarkably, the mean lifetimes of **14** and **16**, which exhibit a 3D tetragonal structure, are significantly enhanced compared to those of **12** and **13**. These results suggest that our approach to controlling the supramolecular structure of rod–coil molecules by variation of coil-to-rod volume fraction can provide a strategy to regulate solid-state photophysical properties such as fluorescence of conjugated molecules.

Experimental

Techniques: ^{1}H NMR spectra were recorded from $CDCl_3$ solutions on a Bruker AM 250 spectrometer. The purity of the products was checked by thin layer chromatography (TLC; Merck, silica gel 60). A Perkin Elmer DSC-7 differential scanning calorimeter equipped with a 1020 thermal analysis controller was used to determine the thermal transitions, which were reported as the maxima and minima of their endothermic or exothermic peaks. In all cases, the heating and cooling rates were 10 °C min^{-1}. A Nikon Optiphot 2-pol optical polarized microscope (magnification 100×) equipped with a Mettler FP 82 hot-stage and a Mettler FP 90 central processor was used to observe the thermal transitions and to analyze the anisotropic texture. Microanalyses were performed with a Perkin Elmer 240 elemental analyzer at the Organic Chemistry Research Center, Sogang University, Seoul, Korea. X-ray scattering measurements were performed in transmission mode with synchrotron radiation at the 3C2 X-ray beam line at Pohang Accelerator Laboratory, Korea. Molecular weight distributions (M_w/M_n) were determined by gel permeation chromatography (GPC) with a Waters R401 instrument equipped with Stragel HR 3, 4, and 4E columns, M7725i manual injector, column heating chamber, and 2010 Millennium data station. Measurements were made using a UV detector and $CHCl_3$ as solvent (1.0 mL min^{-1}). The molecular density (ρ) measurements were performed in an aqueous sodium chloride solution at 25 °C. Optical absorption spectra were obtained with a Shimadzu 1601 UV spectrometer. The steady-state fluorescence spectra were obtained with a Hitachi F-4500 fluorescence spectrophotometer. Time-resolved fluorescence decay measurements were performed using the time-correlated single-photon counting (TCSPC) technique. The exciting system consists of a cavity dumped dual-jet dye laser (700 series, Coherent), synchronously pumped by a Nd:YAG laser (Antares 76-YAG, Coherent). The total mean fluorescence lifetimes (τ_m) were calculated according to

$$\tau_m = \sum_j A(\lambda_j)\tau_m(\lambda_j) / \sum_j A(\lambda_j) \quad (1)$$

through the time-dependent fluorescence intensity $I(t)$ and the mean fluorescence lifetime $\tau_m(\lambda_j)$ at a emission wavelength of λ_j [17], where

$$A(\lambda_j)\tau_m(\lambda_j) = \int_0^\infty A(\lambda_j)\exp[-t/\tau_m(\lambda_j)]dt = I(\lambda_j) \quad (2)$$

$A(\lambda_j)$ is the amplitude of an exponential decay component (i) at an emission wavelength of λ_j and $I(\lambda_j)$ ist the steady-state fluorescence intensity at wavelength λ_j.

Synthesis: A general outline of the synthetic procedure is shown in Scheme 1.

*Synthesis of Compounds **1**–**5***: Compounds **1–5** were all synthesized using the same procedure. A representative example is described for **1**. Tosylated poly(propylene oxide) monomethyl ether (2.5 g, 6.9 mmol), 4′-hydroxymethyl-biphenyl-4-ol (2.7 g, 13.8 mmol), and excess K_2CO_3 were dissolved in 250 mL of ethanol. The mixture was heated at reflux for 24 h. The resulting solution was poured into water and extracted with ethyl acetate. The ethyl acetate solution

  0935-9648/01/1809-1366 $ 17.50+.50/0

was washed with water, dried over anhydrous magnesium sulfate, and filtered. Solvent was removed in a rotary evaporator, and the crude product was purified by column chromatography (silica gel, ethyl acetate/methylene chloride = 1:4 eluent) to yield 2.3 g (85 %) of a colorless liquid.

Compound ***1***: Yield 85 %; ^{1}H NMR (250 MHz, $CDCl_3$, δ [ppm]) 7.55–7.38 (m, 6Ar–H, *m* to $OCH(CH_3)$ and *o* to CH_2OH, *m* to OCH_2OH), 7.00–6.96 (d, J = 8.5 Hz, 2Ar–H, *o* to $OCH_2CH(CH_3)$), 4.58–4.53 (m, phenyl$OCH_2CH(CH_3)$), 3.65–3.32 (m, $OCH_2CH(CH_3)$ and OCH_3), 1.35–1.13(m, 9H, $CH(CH_3)O$).

Compound ***2***: Yield 88 %; ^{1}H NMR (250 MHz, $CDCl_3$, δ [ppm]) 7.54–7.38 (m, 6Ar–H, *m* to $OCH(CH_3)$ and *o* to CH_2OH, *m* to OCH_2OH), 6.99–6.96 (d, J = 8.4 Hz, 2Ar–H, *o* to $OCH_2CH(CH_3)$), 4.56–4.51 (m, phenyl$OCH_2CH(CH_3)$), 3.66–3.36 (m, $OCH_2CH(CH_3)$ and OCH_3), 1.34–1.12 (m, 9H, $CH(CH_3)O$).

Compound ***3***: Yield 82 %; ^{1}H NMR (250 MHz, $CDCl_3$, δ [ppm]) 7.55–7.38 (m, 6Ar–H, *m* to $OCH(CH_3)$ and *o* to CH_2OH, *m* to OCH_2OH), 7.00–6.97 (d, J = 8.4 Hz, 2Ar–H, *o* to $OCH_2CH(CH_3)$), 4.57–4.52 (m, phenyl$OCH_2CH(CH_3)$), 3.74–3.41 (m, $OCH_2CH(CH_3)$ and OCH_3), 1.35–1.07 (m, 9H, $CH(CH_3)O$).

Compound ***4***: Yield 86 %; ^{1}H NMR (250 MHz, $CDCl_3$, δ [ppm]) 7.55–7.38 (m, 6Ar–H, *m* to $OCH(CH_3)$ and *o* to CH_2OH, *m* to OCH_2OH), 7.00–6.97 (d, J = 8.4 Hz, 2Ar–H, *o* to $OCH_2CH(CH_3)$), 4.57–4.50 (m, phenyl$OCH_2CH(CH_3)$), 3.66–3.31 (m, $OCH_2CH(CH_3)$ and OCH_3), 1.35–1.07 (m, 9H, $CH(CH_3)O$).

Compound ***5***: Yield 82 %; ^{1}H NMR (250 MHz, $CDCl_3$, δ [ppm]) 7.55–7.38 (m, 6Ar–H, *m* to $OCH(CH_3)$ and *o* to CH_2OH, *m* to OCH_2OH), 7.00–6.96 (d, J = 8.5 Hz, 2Ar–H, *o* to $OCH_2CH(CH_3)$), 4.56–4.51 (m, phenyl$OCH_2CH(CH_3)$), 3.66–3.37 (m, $OCH_2CH(CH_3)$ and OCH_3), 1.35–1.07 (m, 9H, $CH(CH_3)O$).

Synthesis of Compounds ***6–10***: Compounds **6–10** were all synthesized using the same procedure. A representative example is described for **6**. Compound **1** (2.3 g, 5.9 mmol) was dissolved in 150 mL of methylene chloride. PCC (3.8 g, 17.7 mmol) was added under nitrogen. The reaction mixture was stirred at room temperature under nitrogen for 6 h. The resulting solution was removed in a rotary evaporator, and the crude product was purified by column chromatography (silica gel, ethyl ether eluent) to yield 1.7 g (74 %) of a colorless liquid.

Compound ***6***: Yield 74 %; ^{1}H NMR (250 MHz, $CDCl_3$, δ [ppm]) 10.02 (s, 1H, phenyl*CH*O), 7.93–7.89 (d, J = 8.3 Hz, 2Ar–H, *o* to CHO), 7.71–7.68 (d, J = 8.3 Hz, 2Ar–H , *m* to CHO), 7.59–7.56 (d, J = 8.3 Hz, 2Ar–H, *o* to phenylCHO) 7.03–7.00 (d, J = 8.3 Hz, 2Ar–H, *m* to phenylCHO), 4.61–4.56 (m, phenyl-$OCH_2CH(CH_3)$), 3.60–3.32 (m, $OCH_2CH(CH_3)$ and OCH_3), 1.36–1.12 (m, 9H, $CH(CH_3)O$).

Compound ***7***: Yield 74 %; ^{1}H NMR (250 MHz, $CDCl_3$, δ [ppm]) 10.02 (s, 1H, phenyl*CH*O), 7.93–7.90 (d, J = 8.3 Hz, 2Ar–H, *o* to CHO), 7.72–7.69 (d, J = 8.2 Hz, 2Ar–H , *m* to CHO), 7.58–7.55 (d, J = 8.3 Hz, 2Ar–H, *o* to phenylCHO) 7.03–7.00(d, J = 8.4 Hz, 2Ar–H, *m* to phenylCHO), 4.60–4.53 (m, phenyl-$OCH_2CH(CH_3)$), 3.59–3.37 (m, $OCH_2CH(CH_3)$ and OCH_3), 1.36–1.12 (m, 9H, $CH(CH_3)O$).

Compound ***8***: Yield 70 %; ^{1}H NMR (250 MHz, $CDCl_3$, δ [ppm]) 10.02 (s, 1H, phenyl*CH*O), 7.92–7.89 (d, J = 8.3 Hz, 2Ar–H, *o* to CHO), 7.73–7.70 (d, J = 8.3 Hz, 2Ar–H, *m* to CHO), 7.58–7.56 (d, J = 8.2, 2Ar–H, *o* to phenylCHO) 7.03–7.00 (d, J = 8.3 Hz, 2Ar–H, *m* to phenylCHO), 4.62–4.54 (m, phenyl-$OCH_2CH(CH_3)$), 3.56–3.32 (m, $OCH_2CH(CH_3)$ and OCH_3), 1.36–1.11 (m, 9H, $CH(CH_3)O$).

Compound ***9***: Yield 78 %; ^{1}H NMR (250 MHz, $CDCl_3$, δ [ppm]) 10.02 (s, 1H, phenyl*CH*O), 7.93–7.91 (d, J = 8.2 Hz, 2Ar–H, *o* to CHO), 7.72–7.70 (d, J = 8.2 Hz, 2Ar–H , *m* to CHO), 7.58–7.56 (d, J = 8.2 Hz, 2Ar–H, *o* to phenylCHO) 7.03–7.00 (d, J = 8.3 Hz, 2Ar–H, *m* to phenylCHO), 4.58–4.53 (m, phenyl-$OCH_2CH(CH_3)$), 3.74–3.37 (m, $OCH_2CH(CH_3)$ and OCH_3), 1.37–1.11 (m, 9H, $CH(CH_3)O$).

Compound ***10***: Yield 71 %; ^{1}H NMR (250 MHz, $CDCl_3$, δ [ppm]) 10.02 (s, 1H, phenyl*CH*O), 7.92–7.89 (d, J = 8.3 Hz, 2Ar–H, *o* to CHO), 7.71–7.68 (d, J = 8.3 Hz, 2Ar–H, *m* to CHO), 7.57–7.53 (d, J = 8.4 Hz, 2Ar–H, *o* to phenylCHO), 7.03–6.99 (d, J = 8.3 Hz, 2Ar–H, *m* to phenylCHO), 4.57–4.55 (m, phenyl-$OCH_2CH(CH_3)$), 3.73–3.36 (m, $OCH_2CH(CH_3)$ and OCH_3), 1.35–1.11 (m, 9H, $CH(CH_3)O$).

Synthesis of Compound ***11***: 4,4′-Bis(bromomethyl) biphenyl (0.5 g, 1.48 mmol) was dissolved in 50 mL dry tetrahydrofuran (THF). Triethyl phosphite (0.76 mL, 4.44 mmol) was added under nitrogen. The mixture was heated at reflux for 24 h. The solution was monitored by TLC until completion. The resulting solution was crystallized from hexane, and the crystals were filtered and collected. Filtration of the reaction mixture provided a white solid in 0.44 g (75 %) yield. Yield 75 %; T_m =112 °C; ^{1}H NMR (250 MHz, $CDCl_3$, δ [ppm]) 7.54–7.52 (d, J = 8.3 Hz, 2Ar–H, *m* to $CH_2PO(OCH_2CH_3)_2$), 7.37–7.34 (d, J = 8.4 Hz, 2Ar–H, *o* to $CH_2PO(OCH_2CH_3)_2$), 4.09–3.98 (m, $CH_2PO(OCH_2CH_3)_2$), 3.22–3.14 (d, J = 20 Hz, 2H, $CH_2PO(OCH_2CH_3)_2$), 1.29–1.23 (m, $CH_2PO(OCH_2CH_3)_2$).

Synthesis of Coil–Rod–Coil Molecules ***12–16***: Coil–rod–coil molecules **12–16** were all synthesized using the same procedure. A representative example is described for **12**. Compound **6** (0.8 g, 2.1 mmol) was dissolved in 50 mL dry THF. A solution of **11** (0.15 g, 0.4 mmol) and $KOC(CH_3)_3$ (0.25 g, 2.2 mmol) in 30 mL dry THF was added under nitrogen. The reaction mixture was stirred at room temperature under nitrogen for 24 h. The resulting solution was removed in a rotary evaporator. The crude product was extracted with methylene chloride and water. The methylene chloride solution was washed with water, dried over anhydrous magnesium sulfate, and filtered. The solvent was removed in a rotary evaporator, and the crude product was purified by column chromatography (silica gel, ethyl acetate eluent) to yield 0.4 g (48 %) of a yellow green solid.

Compound ***12***: Yield 48 %; ^{1}H NMR (250 MHz, $CDCl_3$, δ [ppm]) 7.67–7.52 (m, 20Ar–H, *o* to CHCHphenyl, *m* to CHCHphenyl, *o* to phenylOCH_2CH or phenyl$OCH(CH_3)$, *m* to phenylOCH_2CH or phenyl$OCH(CH_3)$), 7.18 (s, 4H, C*H*phenyl), 7.02–6.99 (d, J = 8.4 Hz, 4H, *o* to OCH_2CH or $OCH(CH_3)$), 4.63–4.56 (m, phenyl$OCH_2CH(CH_3)$), 3.70–3.35 (m, 12H, $OCH_2CH(CH_3)$ and OCH_3) 1.36–1.13 (m, 9H, $CH(CH_3)O$); M_w/M_n = 1.02 (GPC); Anal. Calcd. for $C_{60}H_{70}O_8$: C 76.82, H 6.82. Found C 76.79, H 6.81.

Compound ***13***: Yield 42 %; ^{1}H NMR (250 MHz, $CDCl_3$, δ [ppm]) 7.67–7.52 (m, 20Ar–H, *o* to CHCHphenyl, *m* to CHCHphenyl, *o* to phenylOCH_2CH or phenyl$OCH(CH_3)$, *m* to phenylOCH_2CH or phenyl$OCH(CH_3)$), 7.18 (s, 4H, C*H*phenyl), 7.02–6.98 (d, J = 8.5 Hz, 4H, *o* to OCH_2CH or $OCH(CH_3)$), 4.59–4.52(m, phenyl$OCH_2CH(CH_3)$), 3.79–3.37 (m, 12H, $OCH_2CH(CH_3)$ and OCH_3) 1.36–1.13 (m, 9H, $CH(CH_3)O$); M_w/M_n = 1.03 (GPC); Anal. Calcd. for $C_{84}H_{118}O_{16}$: C 72.91, H 8.91. Found C 72.75, H 8.97.

Compound ***14***: Yield 48 %; ^{1}H NMR (250 MHz, $CDCl_3$, δ [ppm]) 7.63–7.52 (m, 20Ar–H, *o* to CHCHphenyl, *m* to CHCHphenyl, *o* to phenylOCH_2CH or phenyl$OCH(CH_3)$, *m* to phenylOCH_2CH or phenyl$OCH(CH_3)$), 7.18 (s, 4H, C*H*phenyl), 7.02–6.99 (d, J = 8.2 Hz, 4H, *o* to OCH_2CH or $OCH(CH_3)$), 4.58–4.53 (m, phenyl$OCH_2CH(CH_3)$), 3.55–3.37 (m, 12H, $OCH_2CH(CH_3)$ and OCH_3), 1.37–1.12 (m, 9H, $CH(CH_3)O$); M_w/M_n = 1.07 (GPC); Anal. Calcd. for $C_{120}H_{190}O_{28}$: C 69.27, H 9.20. Found C 69.31, H 9.36.

Compound ***15***: Yield 35 %; ^{1}H NMR (250 MHz, $CDCl_3$, δ [ppm]) 7.63–7.52 (m, 20Ar–H, *o* to CHCHphenyl, *m* to CHCHphenyl, *o* to phenylOCH_2CH or phenyl$OCH(CH_3)$, *m* to phenylOCH_2CH or phenyl$OCH(CH_3)$), 7.18 (s, 4H, C*H*phenyl), 7.02–6.98 (d, J = 8.4 Hz, 4H, *o* to OCH_2CH or $OCH(CH_3)$), 4.56–4.54 (m, phenyl$OCH_2CH(CH_3)$), 3.75–3.37 (m, 12H, $OCH_2CH(CH_3)$ and OCH_3), 1.36–1.12 (m, 9H, $CH(CH_3)O$); M_w/M_n = 1.07 (GPC); Anal. Calcd. for $C_{138}H_{226}O_{34}$: C 68.23, H 9.38. Found C 69.24, H 9.37.

Compound ***16***: Yield 39 %; ^{1}H NMR (250 MHz, $CDCl_3$, δ [ppm]) 7.63–7.52 (m, 20Ar–H, *o* to CHCHphenyl, *m* to CHCHphenyl, *o* to phenylOCH_2CH or phenyl$OCH(CH_3)$, *m* to phenylOCH_2CH or phenyl$OCH(CH_3)$), 7.18 (s, 4H, C*H*phenyl), 7.02–6.99 (d, J = 8.2 Hz, 4H, *o* to OCH_2CH or $OCH(CH_3)$), 4.56–4.52 (m, phenyl$OCH_2CH(CH_3)$), 3.54–3.37 (m, 12H, $OCH_2CH(CH_3)$ and OCH_3), 1.36–1.12 (m, 9H, $CH(CH_3)O$); M_w/M_n = 1.06 (GPC); Anal. Calcd. for $C_{168}H_{286}O_{44}$: C 67.04, H 9.58. Found C 67.01, H 9.75

Received: November 20, 2000
Final version: May 17, 2001

[1] M. Muthukumar, C. K. Ober, E. L. Thomas, *Science* **1997**, *277*, 1225.
[2] S. Förster, M. Antonietti, *Adv. Mater.* **1998**, *10*, 195.
[3] M. Lee, D.-W. Jang, Y.-S. Kang, W.-C. Zin, *Adv. Mater.* **1999**, *11*, 1018.
[4] a) L. H. Radzilowski, S. I. Stupp, *Macromolecules* **1994**, *27*, 7747. b) S. I. Stupp, V. LeBonheur, K. Walker, L. S. Li, K. E. Huggins, M. Kesser, A. Amstutz, *Science* **1997**, *276*, 384.
[5] P. Leclere, A. Calderone, D. Marsitzky, V. Francke, Y. Geerts, K. Müllen, J.-L. Brédas, R. Lazzaroni, *Adv. Mater*. **2000**, *12*, 1042.
[6] a) M. Lee, B.-K. Cho, H. Kim, J.-Y. Yoon, W.-C. Zin, *J. Am. Chem. Soc*. **1998**, *120*, 9168. b) M. Lee, B.-K. Cho, H. Kim, W.-C. Zin, *Angew. Chem. Int. Ed.* **1998**, *37*, 638. c) M. Lee, N.-K. Oh, W.-C. Zin, *Chem. Commun*. **1996**, 1787.
[7] M. Lee, D.-W. Lee, B.-K. Cho, J.-Y. Yoon, W.-C. Zin, *J. Am. Chem. Soc*. **1998**, *120*, 13 258.
[8] M. Lee, B.-K. Cho, Y.-G. Jang, W.-C. Zin, *J. Am. Chem. Soc*. **2000**, *122*, 7449.
[9] A. Kraft, A. C. Grimsdale, A. B. Holmes, *Angew. Chem. Int. Ed.* **1998**, *37*, 402.
[10] B. Strehmel, A. M. Starker, J. H. Malpert, V. Strehmel, H. Seifert, D. C. Neckers, *J. Am. Chem. Soc*. **1999**, *121*, 1226.
[11] a) M. A. Hempenius, B. M. W. Langeveld-Voss, J. A. E. H. Van Haare, R. A. J. Janssen, S. S. Sheiko, J. P. Spatz, M. Moeller, E. W. Meijer, *J. Am. Chem. Soc.* **1998**, *120*, 2798. b) H. Wang, H. Hau Wang, V. S. Urban, K. C. Littrell, P. Thiyagarajan, L. Yu, *J. Am. Chem. Soc*. **2000**, *122*, 6855.
[12] S. A. Jenecke, X. L. Chen, *Science* **1998**, *279*, 1903.
[13] G. N. Tew, M. U. Pralle, S. I. Stupp, *J. Am. Chem. Soc*. **1999**, *121*, 9852.
[14] R. C. Smith, W. M. Fischer, D. L. Gin, *J. Am. Chem. Soc*. **1997**, *119*, 4092.
[15] H. Meier, M. Lehmann, *Angew. Chem. Int. Ed*. **1998**, *37*, 643.

  0935-9648/01/1809-1367 $ 17.50+.50/0

ADVANCED MATERIALS

[16] Considering the fitted time-dependent fluorescence $I(t)$ and the calculated mean lifetime at a fixed emission wavelength [$\tau_m(\lambda_j)$] [17], the total mean lifetime τ_m corresponding to the steady-state fluorescence spectrum was calculated according to Equations 1 and 2 (see Experimental section).
[17] J. Duhamel, A. S. Jones, T. J. Dickson, *Macromolecules* **2000**, *33*, 6344.
[18] This trend may also arise from the different intermolecular interactions between the adjacent conjugated rods with the variation in the length of the coil segment [19]. However, the 3D confinement effect of the domains seems to be more important in the fluorescence enhancement of these supramolecular materials, as evidenced by density measurements of the rod segments.
[19] a) G. Rumbles, I. D. W. Samuel, C. J. Collison, P. F. Miller, S. C. Maratti, A. B. Holmes, *Synth. Met.* **1999**, *101*, 158. b) S. C. J. Meskers, R. A. J. Janssen, J. E. M. Haverkort, J. H. Wolter, *Chem. Phys.* **2000**, *260*, 415.

Confined Surface Plasmons in Gold Photonic Nanocavities**

By *M. Caterina Netti*, *Steve Coyle*, *Jeremy J. Baumberg*,* *Mohammed A. Ghanem*, *Peter R. Birkin*, *Phil N. Bartlett*, and *David M. Whittaker**

The interaction of light with metals is strongly enhanced by texturing their surface on the scale of the optical wavelength. Normally highly reflecting, metals in sub-micrometer architectures such as spheres can show strong absorptions in the visible spectrum[1–3] due to resonant charge oscillations termed plasmons. However, it is non-trivial to size-select and support such metal spheres in solids. Here we demonstrate a simple scheme to produce large-area colored metal surfaces by completely confining surface plasmons inside gold spherical nanocavities. In contrast to periodic patterning of dielectrics,[4] metals,[5,6] or metallodielectrics,[7] which can produce photonic crystals, here the negative nanocavity curvature localizes the electromagnetic fields into small volumes which can be arranged non-periodically. The microstructured surfaces are formed in a process analogous to "lost wax" casting, by the electrochemical deposition of gold through a template of self assembled latex spheres, generating a wide variety of confining geometries over extended areas of a mechanically robust film. Sharp quantized plasmon resonances are observed in the specular reflection spectra, which correspond to solutions of Maxwell's equations in a spherical metallic void. Unlike spheres, voids couple strongly to incident light with resonant wavelengths which are widely tunable through the growth morphology, but are omnidirectional. Such nanostructures enable new optical interactions in reduced dimensions and provide cost-effective tunable spectral filters.

The metallic microstructures were cast by electrochemical deposition through the pores of an array of sub-micrometer polystyrene latex spheres. These were initially crystallized onto a gold-coated glass slide from colloidal solution.[8,9] The resulting metallic mesh reflects the order of the self-assembled template, allowing convenient control of the pore diameters and local crystalline order. Measurement of the total charge passed allows accurate deposition of the required metal thickness, after which the template can be dissolved in toluene. This last step can be carried out without the shrinkage previously found to cause cracking.[10] Extending our previous work[8] to gold nanotextured films, we are now able to devise new geometries for optical plasmon confinement.

By preparing a sample that is graded in thickness, the electrochemical growth can be followed using scanning electron micrographs of the top surface (Fig. 1). Initially the gold forms a hemispherical cavity (i–iv), but the diffusion-reaction limited nature of the aggregation is geometrically hindered by the next layer of latex spheres, which prevents the cavity from completely closing. Instead a three-fold symmetric pattern of interlinked holes form (v–x) connecting the next hemispherical cavities to the layer below. This mesostructure is repeated in subsequent layers above.

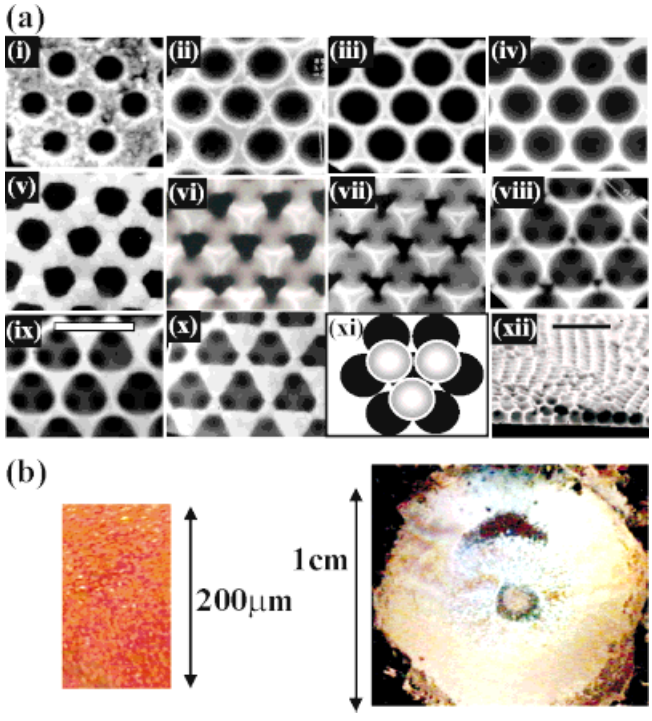

Fig. 1. a) Scanning electron micrographs of the photonic gold nanostructures fabricated with d = 700 nm latex spheres. The thickness varies continuously across the sample: i) 50 nm, iv) 350 nm, vii) 700 nm, x) 1100 nm (scale bar is 1 μm). xi) The lowest void layer (black) and second layer (gray). xii) Cross section (scale bar is 5 μm). b) Diffuse scatter from the sample surface under white light illumination, exhibiting color changes for different thickness. Left: 100 μm × 200 μm area of uniformly 500 nm thick d = 500 nm sample. Right: 1 cm × 1 cm image of a d = 700 nm graded sample—larger crystallites are visible in the center.

[*] Prof. J. J. Baumberg, Dr. M. C. Netti, S. Coyle
Department of Physics and Astronomy, University of Southampton
SO17 1BJ (UK)
E-mail: j.j.baumberg@soton.ac.uk
M. A. Ghanem, Dr. P. R. Birkin, Prof. P. N. Bartlett
Department of Chemistry, University of Southampton
SO17 1BJ (UK)
Dr. D. M. Whittaker
Toshiba Research Europe Ltd
Cambridge, CB4 4WE (UK)

[**] We thank George Attard, Bill Brocklesby, and Jeremy Frey for discussions, the Southampton NanoMaterials Forum, HEFCE JR98SOBA, and EPSRC GR/N37261 for support. MAH thanks the Embassy of the Arab Republic of Egypt, Educational and Cultural Bureau, London, for financial support.

  0935-9648/01/1809-1368 $ 17.50+.50/0